\$ SUPER

Contents lists available at ScienceDirect

Nano Energy

journal homepage: www.elsevier.com/locate/nanoen





Weakly solvating ester electrolyte for high voltage sodium-ion batteries

Rishivandhiga Jayakumar ^{a,b}, Travis P. Pollard ^{c,*}, Oleg Borodin ^c, Vadim Shipitsyn ^{a,b}, Chanmonirath (Michael) Chak ^{a,b}, Glenn Pastel ^{c,*}, Allen Zheng ^d, Michel Johnson ^e, Fuead Hasan ^f, Christopher M. Bejger ^f, Marshall A. Schroeder ^c, Steve G. Greenbaum ^d, Wenhua Zuo ^g, Lin Ma ^{a,b,**}

- a Department of Mechanical Engineering and Engineering Science, The University of North Carolina at Charlotte, Charlotte, NC 28223, USA
- b Battery Complexity, Autonomous Vehicle and Electrification (BATT CAVE) Research Center, The University of North Carolina at Charlotte, Charlotte, NC 28223, USA
- ^c Battery Sciences Branch, DEVCOM Army Research Laboratory, Adelphi, MD 20783, USA
- ^d Department of Physics, Hunter College, City University of New York, New York, NY, USA
- ^e Department of Physics and Atmospheric Science, Dalhousie University, Halifax, NS B3H 4R2, Canada
- f Department of Chemistry, The University of North Carolina at Charlotte, Charlotte, NC 28223, USA
- g Chemical Sciences and Engineering Division, Argonne National Laboratory, 9700 S Cass Ave, Lemont, IL 60439, USA

ARTICLE INFO

Keywords: Non-aqueous sodium-ion batteries Electrolyte solvent Ethyl acetate Failure mechanism

ABSTRACT

Ethyl acetate (EA) was identified as a promising electrolyte solvent for sodium-ion batteries (SIBs), exhibiting low viscosity, cost-effectiveness, and low toxicity. Despite a significant portion of aggregation being linked to the weak solvation of Na $^+$ /EA as revealed by molecular dynamics (MD) simulations, pulsed-field gradient nuclear magnetic resonance (pfg-NMR) analysis identified a noteworthy Na $^+$ diffusion coefficient of 3.95×10^{-10} m² s $^{-1}$ at 25° C in the presence of 1 m NaPF6 salt. Employing fluoroethylene carbonate (FEC) as a film-forming additive to create electrode-electrolyte interphase, this electrolyte surprisingly made \sim 210 mAh Na0.97Ca0.03[Mn0.39-Fe0.31Ni0.22Zn0.08]O2 (NCMFNZO)/hard carbon (HC) pouch cells achieve a lengthy cycling lifetime of 250 cycles with \sim 80 % capacity retention, cycled up to 4.0 V at 40°C. X-ray photoelectron spectroscopy (XPS) revealed increasing interphasial organic species over cycling, augmenting charge transfer resistance on both cathode and anode, particularly during fast charging or low temperatures (<10°C), promoting Na plating. Gas chromatography-mass spectrometry combined with density functional theory identified CO2 as the major gas generated from charged cathode/electrolyte interactions, exhibiting temperature/voltage dependence.

1. Introduction

Decreasing atmospheric greenhouse gas levels is crucial to mitigate climate change impacts like wildfires, extreme weather, and ocean acidification. Transitioning from fossil fuels to renewable energy sources is a key priority. Lithium-ion batteries (LIBs) play a significant role in this transition, widely used in grid-scale energy storage and electric vehicles (EVs) due to their durability, high energy density, and decreasing costs [1,2]. However, the rapidly increasing energy demands highlight the needs for reliable, cost-effective electrochemical energy storage systems to alleviate the lithium and other rare transition metal resource constraint [3,4].

Sodium-ion batteries (SIBs) have emerged as promising alternatives to complement LIB technology, especially in applications where cell energy density is not the primary concern, such as grid energy storage systems and low speed vehicles. The abundance of sodium and the development of electrode materials using inexpensive and widely available elements like carbon, copper, manganese, and iron contribute to the appeal of SIBs [5–7]. To better meet the requirements of grid energy storage systems and low-speed vehicles, SIBs must be engineered to have longer calendar life, extended cycling lifetime, wider temperature operation range, and reduced cost. Achieving these enhancements may involve incorporating new cathode and/or anode materials, as well as implementing rational electrolyte design strategies [8–11]. However,

E-mail addresses: travis.p.pollard.civ@army.mil (T.P. Pollard), glenn.r.pastel.civ@army.mil (G. Pastel), l.ma@charlotte.edu (L. Ma).

^{*} Corresponding authors.

^{**} Corresponding author at: Department of Mechanical Engineering and Engineering Science, The University of North Carolina at Charlotte, Charlotte, NC 28223, USA.

most demonstrations of these material and strategy modifications are confined to coin cell tests [12,13], lacking validation in multilayer pouch cells. This limitation makes it challenging to identify cell failure mechanisms such as gas evolution [14,15] and sodium plating [16,17], effectively turning them into black boxes.

Esters, particularly ethyl acetate (EA), have garnered significant research interest in LIBs as co-solvents or even sole solvents [18–22]. This is because they can enhance the physical properties of traditional carbonate-based electrolytes by offering low freezing points and low viscosity. Esters have been explored for their potential in low-temperature applications of Li-ion cells, and they also offer cost-effectiveness [20,21]. However, the utilization of known film-forming additives like vinylene carbonate (VC) [18,23] and fluoroethylene carbonate (FEC) [24,25] in combination with these esters is essential to passivate the graphite anode and ensure the proper functioning of LIBs. Despite these advancements, there has been no demonstration of the use of sole ester solvents in SIBs, and there is a lack of understanding regarding relevant failure mechanisms in this context.

Here, we utilized FEC as a representative film-forming additive at different concentrations (2 wt%, 5 wt%, and 10 wt%) to demonstrate the feasibility of using EA as the sole weakly solvating solvent in \sim 210 mAh $Na_{0.97}Ca_{0.03}[Mn_{0.39}Fe_{0.31}Ni_{0.22}Zn_{0.08}]O_{2}$ (NCMFNZO)/hard carbon (HC) pouch cells. Despite containing a significant proportion (>50 %) of contract ion pair (CIP) and aggregate (AGG), this electrolyte exhibited exceptional conductivity of 5.28 mS cm⁻¹ and a Na⁺ diffusion coefficient of 3.95×10^{-10} m² s⁻¹ at 25°C. With the formation of solid electrolyte interphase (SEI) and cathode electrolyte interphase (CEI) derived from FEC, NCMFNZO/HC cells achieved a long cycling lifetime of 250 cycles with ~80 % capacity retention cycled between 1.5 and 4.0 V at 40°C. The increase in the charge transfer resistance (R_{ct}) leading to Na plating was identified as the primary cause of Na inventory loss during the long-term cycling, triggering thermal stability concerns at elevated temperatures, particularly during fast charging or at low temperatures. Severe gas generation with CO2 as the major component was observed using Archimedes' principle during high voltage and high-temperature storage and long-term cycling. Density functional theory (DFT) calculations were employed to identify potential pathways for generating CO₂ through the decomposition of FEC or EA. We find that the majority of gas generation after formation results from the reaction between the cathode and electrolytes, and it is influenced by temperature and upper voltage. Higher temperatures and cutoff voltages lead to increased gas generation.

2. Experimental

2.1. Electrode and electrolyte preparation

NCMFNZO/HC dry pouch cells with a capacity of 210 mAh, manufactured by Lifun Technology (Zhuzhou, Hunan), were acquired. Detailed information about the cells can be found in previous reports [25,26]. The active materials of cathode and anode (Figure S1) are loaded at 16 mg cm² and 9.47 mg cm², respectively. Both electrodes use aluminum foil as the current collector, and the active electrode area is approximately 99.58 cm². To obtain the electrodes for symmetric cells fabrication, pouch cells were carefully cut open and the jelly roll was extracted and unrolled to separate the cathode and anode. To obtain single side coated cathodes, N-methyl pyrrolidone (NMP) was used to remove electrode materials from the current collector inside the glovebox. Cathode and anode samples, each sized for coin cells (0.95 cm²), were punched out. Afterward, symmetric 2032-coin cells were assembled using these electrodes, with a single piece of polypropylene blown microfiber (BMF) as the separator, and ${\sim}150~\mu L$ of electrolyte was dispensed into each cell. Molality was used to prepare the electrolytes. 1 m NaPF₆ (> 99.0 %, Capchem) in EA ($H_2O < 20$ ppm, Sigma-Aldrich) was used as a control electrolyte in this work. Electrolytes containing additives were created by dissolving FEC (H₂O < 20 ppm, Gotion) into the control electrolyte at various ratios.

2.2. Electrochemical measurements

The dry pouch cells were filled with 1 g of electrolyte and sealed using a compact vacuum sealer (MSK-115A-111, MTI Corp.). The sealing process was conducted under a gauge pressure of -85 kPa, with a sealing temperature of 165°C and a sealing time of 5 seconds, all performed inside an Ar-filled glove box. During the formation step, all cells were moved to temperature-controlled chambers set at 40 \pm 0.1°C (using Neware Battery Testing System, Shenzhen) and allowed to rest for 3 hours before charging to 4 V at a rate of C/20. Subsequently, the cells were discharged to 3.1 V at C/20 for degassing. After formation, the cells underwent two cycles of discharging to 1.5 V and charging to 4.0 V at a rate of C/20 and 40°C, followed by a 500-hour storage at open circuit voltage. After storage, the cells underwent long-term cycling testing between 1.5 V and 4.0 V at 40°C with a rate of C/3 in constant current constant voltage (CCCV) mode with a C/20 cut-off current. Additionally, a check-up cycle was conducted every 50 cycles at C/20 to examine capacity loss caused by Na inventory loss. In this work, cells designated for testing fast charging capability or low temperature performance commenced cycling immediately after the formation process. Fast charging testing was conducted at 25°C using various charging rates, including C/3, 1 C, 2 C, 3 C, and 4 C, while the discharging rate remained at C/3. Each cell underwent 10 cycles under each charging rate condition. For low temperature screening testing, the cells were subjected to the same CCCV conditions as in the long-term cycling step, with temperatures set at -10° C, 0° C, and 10° C. Following screening testing, the cells were cycled at 10°C within the voltage range of 1.5 V to 3.8 V to prevent electrolyte oxidation, employing different charging rates of C/5 and C/2.5 to observe the impact of Na plating on cell failure. Each cell underwent 40 cycles under each charging rate, with C/3 during discharge. The electrochemical impedance spectroscopy (EIS) data, obtained with a Biologic VMP3, included ten data points per decade spanning from 100 kHz to 100mHz. The signal amplitude was set at 10 mV, and measurements were conducted at 25°C.

2.3. Cells and materials characterization

The gas generated in the pouch cells or pouch bags during formation, storage, and cycling was quantified using Archimedes' principle, as outlined in the study by Aiken et al. [27]. Gas chromatography-mass spectrometry (GC-MS) was used to analyze the gases generated in the pouch cells. The gas extraction and analysis procedure can be referred to the previous report [28]. 200 µL of the gas was injected into an Agilent 7890 gas chromatograph coupled to an Agilent 5977B single-quadrupole mass spectrometer for analysis. During accelerating rate calorimetry (ARC) measurements, two pouch cells were wrapped around the thermocouple of an accelerating rate calorimeter (EV+, Thermal Hazard Technology). ARC testing was monitored under adiabatic conditions, triggered when the sample's self-heating rate (SHR) exceeded 0.02 °C/min. Data collection for ARC was performed within the temperature range of 50°C to 315°C, with a heating step of 5.0°C/step. Experiments were programmed to halt automatically if the temperature exceeded 350°C or if the SHR surpassed 10 °C/min. Infrared (IR) spectra were collected for selected electrolytes in an attenuated total internal reflection (ATR) geometry using a Spectrum 100 spectrometer (PerkinElmer) with a diamond ATR setup. The spectra were the average of 64 scans collected at a resolution of 2 cm⁻¹. The self-diffusion coefficients of 1H , ^{19}F , ^{23}Na (D_H , D_F , and D_{Na} , respectively), related to the hydrogen in the EA or propylene carbonate (PC), the fluorine in the PF₆ anion, and the sodium ion, were measured with a Varian/Agilent 300 MHz WB NMR spectrometer equipped with a DOTY z-gradient probe, with Larmor frequencies at 300 MHz, 282.4 MHz, and 79.4 MHz, respectively. A spin-echo sequence was used with gradient pulse durations (δ) of 2 ms, diffusion delay durations (Δ) of 5–10 ms, and

gradient field strength (g) varied from 3 to 900 G cm⁻¹ as needed.

The electrolyte conductivity was measured at room temperature using conductivity meters (Mettler Toledo) after routine calibration with 1.68, 4.00, 7.00, and 10.00 pH solutions. The viscosity of selected electrolytes was assessed at room temperature using an Ostwald viscometer (Sibata, Japan). As the Ostwald viscometer functions as a comparative instrument and cannot directly measure viscosity, water was employed as a calibration standard under atmospheric pressure. NCMFNZO or HC electrodes were obtained from pouch cells in an argon filled glovebox, rinsed with anhydrous dimethyl carbonate (DMC) and dried in an antechamber under vacuum overnight, then transferred into XPS system by a sealed vacuum transfer setup. The XPS data was collected by using a combination of survey scan (pass energy 224 eV, step size 0.4 eV) and high-resolution scan (pass energy 55 eV, step size 0.05 eV). Surface neutralization was achieved using a low energy Ar-ion flow and an electron neutralizer. The X-ray with a power of 25 W was focused to a spot size of $100 \mu m$. XPS spectra peak was fitted with 70/30Gaussian/Lorentzian line shapes on a Shirley background via PHI's Multipak software v. 9.6. All XPS spectra were adjusted relative to the binding energy of 284.8 eV (C1s sp3) to correct for any surface charging offset during the measurement.

2.4. Theoretical modeling

Density functional theory (DFT) calculations of EA and FEC decomposition were performed with Gaussian 16 rev. C.02 [29] package using ωB97XD functional and CBSB7++ basis set with all the complexes being immersed in implicit solvent represented by the SMD(ether) polarized continuum model, denoted as SMD(ether)/ωB97XD/CBSB7++. In some instances the SMD(ether)/G4MP2 composite model chemistry is used as well. Potentials are computed via the half-cell reaction equation, assuming 4.44 V for the absolute potential of the standard hydrogen electrode, $E^{r/o}=\pm\frac{\Delta G(A^{\pm})-\Delta G(A)}{nF}-(4.44-2.71)$. Here, $\Delta G(A^{\pm})$ is the free energy of the reduced or oxidized species taken from DFT, $\Delta G(A)$ is the free energy of the species before reduction or oxidation also taken from DFT, F is Faraday's constant, n is the number of electrons transferred. The potentials reported are the highest (reduction) or lowest (oxidation) computed, in total ~1300 calculations were performed sampling different conformers and complex geometries. The bulk of these were prepared using Crest and the extended tight binding method [30].

Molecular dynamics (MD) simulations were performed on the 1 m NaPF $_6$ in EA, 1 m NaPF $_6$ in EA + 5 wt% FEC and 1 m NaPF $_6$ in PC containing 64 NaPF₆ and 726 EA, 726 EA+64 FEC and 426 PC solvent molecules. The density of 1 m NaPF₆ in EA and 1 m NaPF₆ in PC are 1.01 (MD) 1.02 (exp) g cm $^{-3}$ and 1.30 (MD) 1.25(exp) g cm $^{-3}$, respectively. Two replicas were created for each electrolyte in a gas phase followed by a shrinking simulation box over 1 ns at 333 K for 40 ns. Then, temperature was decreased to 298 K and seven replicas were created by taking different configurations from 333 K runs. Each replica was equilibrated from 8 to 12 ns at 298 K followed by 96 ns - 240 ns runs with total simulation time of 1317 ns for 7 replicas. Two replicas were simulated for 1 m NaPF₆ in EA + 5 wt% FEC for 280 ns and PC/NaPF6 for 40 ns at 298 K. Pure EA and PC solvents were simulated for 20 and 12 ns, respectively. For EA density was 912 (MD) and 902 (exp, wiki) 1196 kg m⁻³, heat of vaporization 8.67 (MD) and 8.51, 8.3 \pm 0.4 (exp [31]) kcal mol⁻¹, viscosity 0.465 (MD) and 0.423 (exp [31]) mPa*s.

PC density was 1196 kg m $^{-3}$ (MD) and 1198.8 kg m $^{-3}$ (exp [32]), heat of vaporization 14.3 (MD) and 14.7 (exp [33]) kcal mol $^{-1}$, viscosity 2.4 (MD) and 2.512 (exp [32]) mPa*s, self-diffusion was 5.4 (MD) and 5.8 (exp [34]) in 10^{-10} m 2 s $^{-1}$.

A many-body polarizable APPLE&P force field [35–38] was extended by refitting $\mathrm{Na}^+/\mathrm{O}(\mathrm{carbonyl})$ repulsion parameters to be between MP2/aug-cc-pvTz and G4MP2 QC values as shown in Figure S2 as was previously done for the carbonate/LiPF₆ force field. It also shows that

Na⁺ binding energy to PC is significantly higher than to EA and FEC.

A time reversible (RESPA) integrator with three-time steps was used in MD simulations: i) bonds and angles to the forces were calculated at any 0.5 femtoseconds (fs), ii) dihedrals and non-bonded forces within 7 Å cut-off was updated at any 1.5 fs, and iii) the remainder of the forces (reciprocal space Ewald using k=83 vectors) and non-bonded forces within 12 Å cut-off was updated at any 3fs, while larger 14 Å cutoff was used PC/NaPF₆. Nose-Hoover thermostat was used for temperature control with the associated frequency of 0.01 fs⁻¹. The induced dipoles (µ) were found self-consistently at each 3fs timestep. Self-diffusion coefficients, viscosity and conductivity were extracted previously described methodology [39] as shown in Figure S2(g-j) yielding the following self-diffusion coefficients: 12.6 (EA), 5.4 (PF₆), 4.7 (Na⁺) in 10^{-10} m² s⁻¹ before hydrodynamic correction of 1.3 0⁻¹⁰ m² s⁻¹, conductivity of 7.6 mS cm⁻¹ and viscosity of 0.96 mPa*s for EA-NaPF₆ at 298 K. For PC/NaPF₆ MD simulations yield self-diffusion coefficients of 1.4 (PC), 1.1 (PF₆) and 0.68 (Na⁺) in 10^{-10} m² s⁻¹

Instead of directly extracting conductivity using Einstein relation given below (Eqs. 1 and 2), the degree of ion uncorrelated motion (ionicity or inverse Haven ratio) was $\alpha_d = H_R^{-1}$ was determined as shown in Figure S2(g) the average of 7 replicas and used together with uncorrelated conductivity $\sigma_{\rm uncorr}$ determined from self-diffusion coefficients (Eq. 3) to determine conductivity using Eq. 4.

$$\sigma = \lim_{t \to \infty} \frac{e^2}{6tVk_{\rm B}T} \sum_{i,j}^{N} z_i z_j \left\langle ([{\rm R}_i(t) - {\rm R}_i(0)])([{\rm R}_j(t) - {\rm R}_j(0)]) \right\rangle \tag{1}$$

$$\sigma = \sigma_{+}^{\text{self}} + \sigma_{-}^{\text{self}} + \sigma_{++}^{\text{d}} + \sigma_{--}^{\text{d}} - 2\sigma_{+-}$$
 (2)

where e is the electron charge, V is the volume of the sample, $k_{\rm B}$ is Boltzmann's constant, T is the temperature and n_+ and n_- are the number of cations and anions, respectively.

In the case when all ions are dissociated, and their motion is uncorrelated the off-diagonal components could be neglected, i. e. $\sigma_{++}^d+\sigma_{--}^d-\sigma_{+-}=0$ and one recovers Nernst-Einstein equation for the uncorrelated conductivity σ_{uncorr} :

$$\sigma_{\rm uncorr} = \frac{e^2}{V k_{\rm B} T} (n_+ D_+ + n_- D_-) \tag{3}$$

Thus, the ratio of conductivity to $\sigma_{\rm uncorr}$ characterizes the degree of ion uncorrelated motion that is also called ionicity or inverse Haven ratio:

$$\alpha_d = H_R^{-1} = \frac{\sigma}{\sigma_{\text{uncorr.}}} = \frac{\sigma_+^{\text{self}} + \sigma_-^{\text{self}} + \sigma_{++}^{\text{d}} + \sigma_{--}^{\text{d}} - 2\sigma_{+-}}{\sigma^{\text{self}}}$$
(4)

Figure S2h shows that the degree of ion uncorrelated motion α_d is 0.23 from MD simulations in accord with experimental value of 0.20. Low α_d is due to significant cation – anion correlations σ_{+-} =0.28 as shown in Figure S2i.

The full matrix of the charge displacement contributions to conductivity could be decomposed to the self-diffusion contributions coming from the diagonal terms $\sigma_+^{\rm self}+\sigma_-^{\rm self}$, the off-diagonal terms arising from the correlation of distinct cation – cations and anion – anion motion $\sigma_{++}^{\rm d}+\sigma_{--}^{\rm d}$ and the off-diagonal distinct anion – anion motion. Transference number in the center of mass frame of reference was estimated from the positive contribution to the full matrix of displacements and is shown in Figure S2h

$$t_{+}^{COM} = \left[\sigma_{+}^{self} + \sigma_{++}^{d} - \sigma_{+-}\right] / \sigma$$
 (5)

Figure S2 indicates t_+^{COM} around 0.3. In our experience, t_+^{COM} requires the longer simulations to converge compared to α_d as shown in Figure S2.

Due to stronger Na $^+$ /PC binding energy compared to Na $^+$ /EA, PC/NaPF $_6$ electrolyte had much higher fraction of free ions (\sim 50 %) compared to around 8.3 % observed for EA/NaPF $_6$.

3. Results and Discussion

The bulk electrolyte structure of EA-based electrolyte was explored using the Fourier transform infrared (FTIR) spectra (Fig. 1a and S3) in combination with molecular dynamics (MD) simulations (Fig. 1b-g and Fig. S2, 4). The C=O stretching mode of EA (\sim 1750 cm⁻¹ for EA) was observed and contrasted with the C=O peak originating from the interaction between Na⁺ and carbonyl. A trivial Na⁺ C=O peak separations can be observed (Fig. 1a), which is consistent with previous FTIR result [40]. Upon the inclusion of 5 wt% FEC additive, a minor red shift was observed in the C \equiv O stretching mode of FEC (\sim 1830 cm $^{-1}$ [41], Figure S3), indicating potential interaction between FEC and Na⁺. This interaction was further validated through MD simulations (Fig. 1d and **S4**). Radial distribution functions (RDFs, Fig. 1d) show that Na⁺ prefers to coordinate carbonyl oxygens of EA with significant contributions from carbonyl oxygens from FEC and fluorine atoms from the PF₆ anions. The Na⁺ cation coordination with non-carbonyl (ether like-) oxygens denoted as EO is rarely observed in accord with quantum chemistry (QC) results (Figure S2). Most EA exist in the trans - trans conformer (Figure S2) that is also the most energetically favorable complex in the gas-phase. Higher probability for Na⁺ to coordinate EA compared to FEC is also consistent with a slightly stronger binding of Na⁺ to EA vs. FEC in gas-phase that is also accurately captured by the force field. A strong Na⁺-P(PF₆) is consistent with strong CIP and AGG formation. In fact, Fig. 1e shows that only around 8 % of ions exist as free ions that do not have counter ion within 5 Å. Most ions ~50 %, according to MD simulation, exist as CIPs and do not contribute to ion transport. Yet, a combination of ~ 10 % of free ions and ~ 16 % of three ion AGGs contribute most to conductivity of 8.56 mS cm⁻¹ in MD and 5.28 mS cm⁻¹ from

experiments for 1 m NaPF₆ in EA. A combination of pfg-NMR (i.e. Na⁺ diffusion coefficient of 3.95×10^{-10} m² s⁻¹, Figures S5-6) and conductivity (i.e. 5.28 mS cm⁻¹) yields degree of ion uncorrelated motion [42] that is often called ionicity of 0.20 from experiments and 0.23 from MD simulations (Figure S2g). As a comparison, much higher ionicity of 0.6 was observed experimentally with a conductivity of 5.65 mS cm⁻¹ for 1 m NaPF₆ in PC (Figure S7), which is a common electrolyte for SIBs, due to strong dissociation of NaPF₆ salt in PC as a result of much stronger Na⁺/PC binding energy compared to Na⁺/EA (Figure S2). The comparison of ionicity between 1 m NaPF₆ in PC and 1 m NaPF₆ in EA could also be inferred using the Walden plot (Figure S8). Further examination of RDFs (Fig. 1d) also indicates that there is small peak around 2.3 Å for Na⁺-F(FEC) resulting in 0.11 of F(FEC) being found near Na⁺. Such configurations are important for enabling reduction of Na⁺-FEC discussed below. MD simulations predicted 1 m NaPF₆ in EA viscosity of 0.96 mPa*s in excellent agreement with the experimentally observed value of 0.83 mPa*s further validating accuracy of the developed force field. Here "weakly solvating electrolyte" is defined by a prevalence of cation-anion pairs (CIP and AGG) rather than a dominance of dissociated species caused by Na⁺-EA interaction. RDFs for PC/NaPF₆ show much smaller Na-F and Na-P peak magnitudes compared to EA/NaPF₆ (Figure S4f, g)

Leveraging NCMFNZO/HC pouch cells, the effect of EA-based electrolytes on cell formation was identified. Different concentrations of FEC including 2 wt%, 5 wt%, and 10 wt% were selected as film-forming additives. With the addition of FEC additive, a charge capacity of \sim 240 mAh was observed during the first charging cycle up to 4.0 V. The irreversible capacity percentages were measured at 15.5 %, 14.9 %, and 15.3 % for FEC concentrations of 2 wt%, 5 wt%, and 10 wt%,

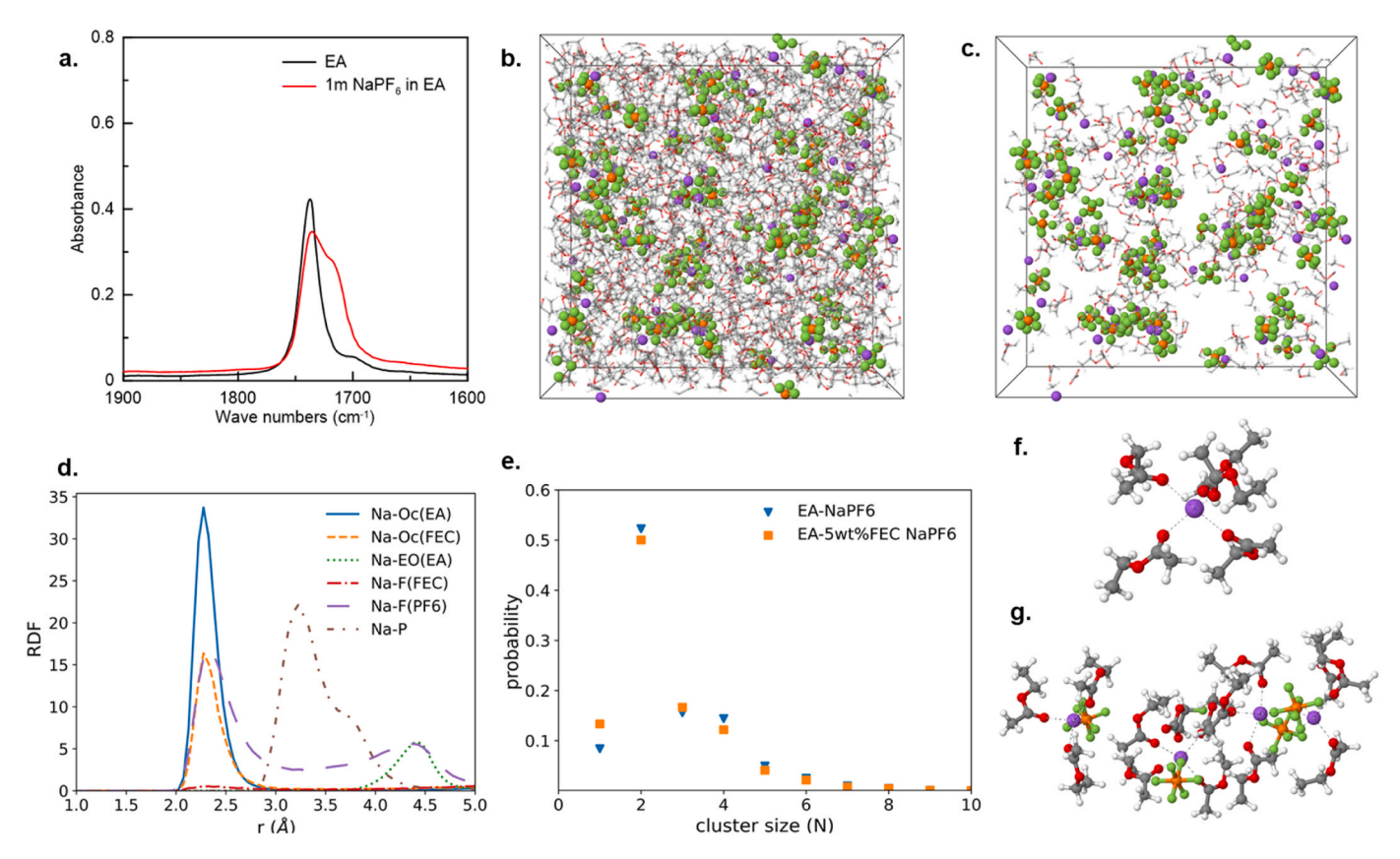


Fig. 1. The analysis of bulk structures of EA-based electrolytes. (a) FTIR analysis of the carbonyl region of selected electrolytes as labeled. (b) A snapshot of MD simulation box of 1 m NaPF₆ in EA with EA solvent shown as wireframe and Na⁺ (purple), PF₆ ions (orange and green) as ball and stick; (c) a simulation box of 1 m NaPF₆ in EA showing only the solvent and anions in the first coordination shell of Na⁺ cations (5.0 Å); (d) radial distribution functions (RDFs) of 1 m NaPF₆ in EA + 5 wt% FEC; (e) probability for an ions to belong to an ion aggregate of size N, N=0 denotes free ions, N=1 denotes ion pairs; (f-g) representative solvates of 1 m NaPF₆ in EA. Additional solvates of 1 m NaPF₆ in EA + 5 wt% FEC are shown in Fig. S4.

respectively (Fig. 2a). Conversely, in the absence of FEC, no discharge capacity was evident after the initial charging cycle (Fig. 2a). Upon closer examination of the differential capacity versus cell potential (dQ/ dV vs. V, Fig. 2b), FEC containing cells exhibit a distinct peak around 1.6 V (HC potential around 1.5 V vs Na/Na⁺) [26], which is consistent with the DFT calculations on the ring-opening and defluorination reactions of FEC in the 1.7 - 1.8 V range (vs Na⁺/Na, Figure S9). Conversely, in the absence of FEC, such a peak is absent. This observation suggests the reduction of FEC occurring on the surface of the HC anode. According to Le Châtelier's principle, chemical reactions are more likely to occur when the concentration of reactants is increased. Therefore, the reduction peak shifts to a lower cell potential (HC at higher potential versus Na⁺/Na) as the concentration of FEC increases. A distinct peak at ~2.3 V is noticeable in the EA cell without FEC, suggesting continuous reduction of EA at the HC surface and the absence of a protective SEI formation. Because NaPF₆ salts tend to aggregate within EA-based electrolytes (Fig. 1), DFT calculations were conducted to determine the reduction potential of the positively charged aggregate species $[Na_2PF_6]^+$ (Figure S9). It was observed that this potential is shifted from 0.5 V in the neutral ion pair to 1.77 V (vs Na^+/Na). However, it seems that the PF_6 -derived SEI, if any, may not provide adequate passivation for the HC anode to ensure its functionality. Consequently, the addition of FEC is required to enhance the SEI's effectiveness.

The gas volume generated during the first charge to 4.0 V was quantified using Archimedes' principle [27]. NCMFNZO/HC pouch cells filled with electrolyte containing different concentrations of FEC produced a significant amount of gas, around 3.5 mL, during this initial charge (Fig. 2c). The absence of a stable SEI without FEC leads to substantial gas generation, damaging the cell and rendering the quantification of gas volume infeasible. Further investigation is necessary to understand the origin of this gas, which likely stems from a combination of reduction and oxidation processes [27]. It may result from the reduction of the electrolyte and/or additive (Figure S9), leading to SEI formation at the HC anode, as well as the oxidation of the electrolyte and/or additive at the NCMFNZO cathode, contributing to the passivation of the cathode. This work will focus on elucidating the impact of

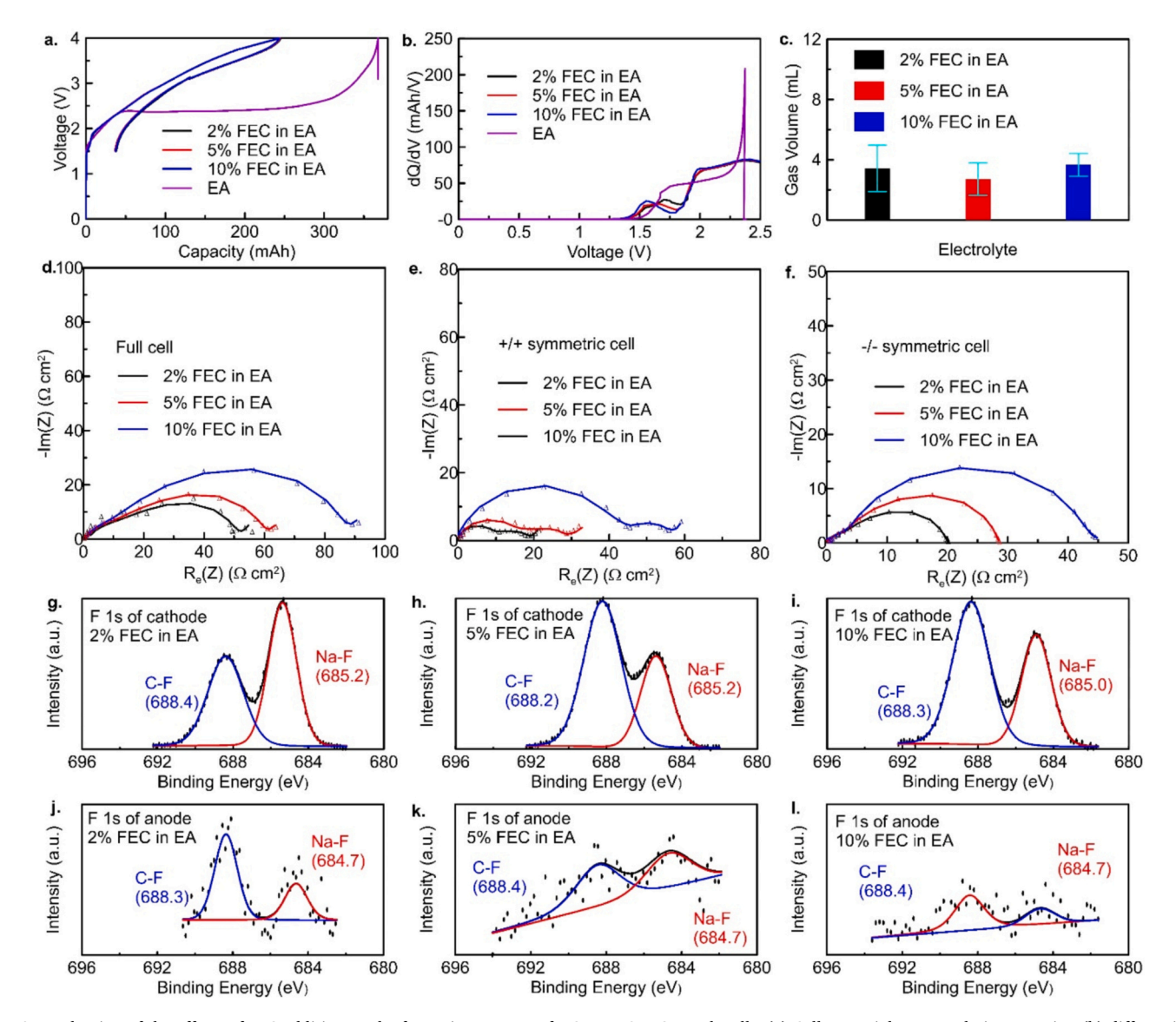


Fig. 2. Evaluation of the effects of FEC additive on the formation process of NCMFNZO/HC pouch cells. (a) Cell potential vs. cumulative capacity; (b) differential capacity vs. cell potential; (c) gas evolution measured at 3.1 V after formation up to 4.0 V; (d) Nyquist plot of the area specific impedance of NCMFNZO/HC pouch cells at 4.0 V after cell formation. Nyquist plot of the half of the area specific impedance of (e) NCMFNZO/NCMFNZO symmetric cells ((-/-)/2) reconstructed from NCMFNZO/HC pouch cells at 4.0 V after formation. All impedance measurements were performed at 25 °C. Experimental data are shown as solid line and fitted data are shown as triangle symbol. Each spectrum are the average results of two cells measurement. XPS spectra of F 1 s for (g-i) NCMFNZO cathode corresponding to (e). XPS spectra of F 1 s for (j-l) HC anode corresponding to (f).

upper cut-off voltage and temperature on gas evolution post-formation, which will be elaborated upon in subsequent discussions.

Evaluating the impact of different concentrations of FEC on the charge transfer resistance (Rct), which signifies the resistance encountered by Na⁺ ions as they pass through the SEI/CEI and enter the active material, was achieved using EIS at 25°C (Fig. 2d-f). In this study, both blocking and non-blocking electrodes, along with an equivalent circuit (Figure S10), were utilized to differentiate between the contribution of R_{ct} and contact resistance. Blocking electrodes are those at 0 % state of charge (SOC), where sodium ions are prevented from intercalating into the electrode material, thus inhibiting charge transfer via faradaic reactions [43,44]. Conversely, non-blocking electrodes, representing charged electrodes, facilitate sodium ion transfer into the active electrode material, enabling faradaic reactions. While temperature has minimal impact on contact resistance, the resistance to charge transfer demonstrates a significant temperature dependency. Through temperature variation, the contact resistance of the NCMFNZO cathode and HC anode has been determined to be 8 $\Omega \times \text{cm}^2$ and 6 $\Omega \times \text{cm}^2$, respectively (Figure S11). According to the Nyquist plot (Fig. 2d) with equivalent circuit fitting (Figure S10, Supplementary Table 1) using the combination of contact resistance value of NCMFNZO cathode and HC anode, the R_{ct} of 10 wt% FEC containing cell is much larger compared to that of 2 wt% and 5 wt% FEC containing cells after formation. To detect if the difference of R_{ct} primarily stems from the cathode or anode, EIS with equivalent circuit fitting was employed for symmetric cells (Fig. 2d-e, Supplementary Table 1). Two symmetric cells were constructed for each electrolyte composition to showcase the repeatability of the results. Upon increasing FEC from 2 wt% to 10 wt%, the primary increase in R_{ct} originates from both the NCMFNZO cathode and the HC anode side simultaneously.

To gain insight into and compare the effects of different concentrations of FEC additive on the electrode/electrolyte interphases, as well as to understand their correlation with the corresponding electrochemical performance, XPS analysis was carried out for both the NCMFNZO cathode (Fig. 2g-i) and HC anode (Fig. 2j-l) after formation. According to the previous report [45], the C 1 s core spectra of NCMFNZO electrodes are predominantly influenced by the presence of PVDF and carbon black. This is attributed to the covering effect of the PVDF binder on the active material and the substantial surface area of the carbon. In the fresh NCMFNZO cathode, the peak observed at 284.5 eV is assigned to sp²-C originating from the carbon black, whereas the peaks at 286.1 and 290.0 eV correspond to -CH₂ and -CF₂- like carbons present in the

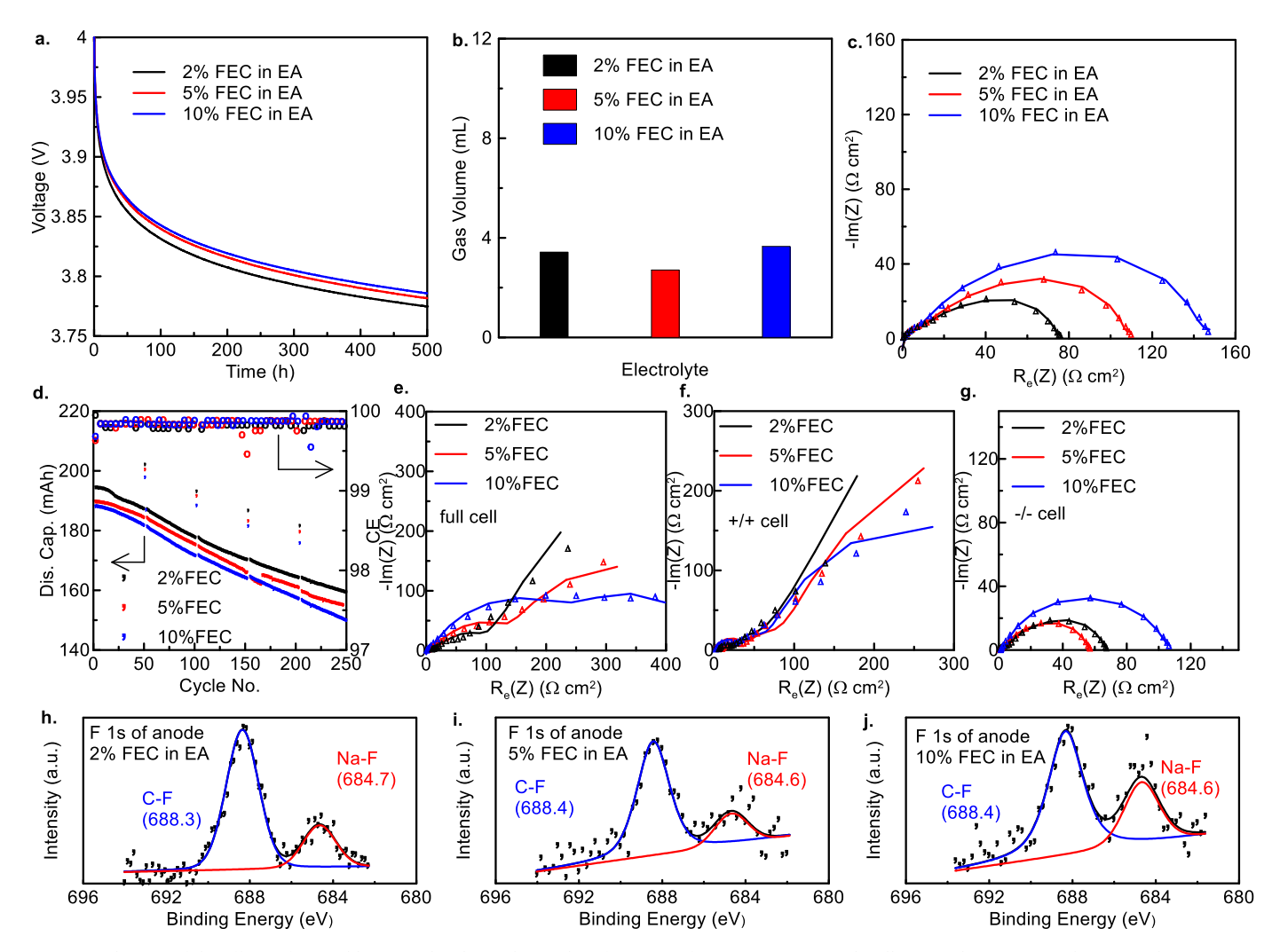


Fig. 3. Evaluation of the effects of FEC additive on the electrochemical performance of NCMFNZO/HC pouch cells. (a) Voltage vs. time during 500 hours storage testing at 40°C and 4 V; (b) gas evolution during 500 hours storage testing; (c) the Nyquist plot after 500 hours storage measured at 3.1 V and 25°C; (d) discharge capacity, and CE vs. cycling No. during long-term cycling between 1.5 and 4 V at 40°C with a rate of C/3 in CCCV mode with a C/20 cut-off current. C/20 was performed every 50 cycles. (e) Nyquist plot of the area specific impedance of NCMFNZO/HC pouch cells at 4.0 V after long-term cycling in (d). Nyquist plot of the half of the area specific impedance of (f) NCMFNZO/NCMFNZO symmetric cells ((+/+)/2) and (g) HC/HC symmetric cells ((-/-)/2) reconstructed from NCMFNZO/HC pouch cells at 4.0 V after long-term cycling. All impedance measurements were performed at 25 °C. Experimental data are shown as solid line and fitted data are shown as triangle symbol. Each spectrum are the average results of two cells measurement. XPS spectra of F 1 s for (h-j) HC anode corresponding to (g).

PVDF binder, respectively (Figure S12) [45]. After formation, the peaks at 287 and 288.9 eV, deconvoluted from the C 1 s core spectra (Figure S13), are potentially attributed to CO_x-like species resulting from the degradation of the FEC additive. This observation aligns with the findings from the O 1 s core spectra analysis (Figure S12-13). In addition to organic species, the F 1 s core spectra (Fig. 2g-i) suggests the formation of NaF₂ in the CEI. When examining the fresh HC anode, the C 1 s core spectra can be broken down to reveal the characteristic peaks of sp^2 -C (284.5 eV), C-C/CH₂- (285.4 eV), and C-O (286.2 eV) [46], while the absence of the F 1 s spectra is due to the absence of a fluorine containing binder (Figure S14). Following formation, the presence of a sharp peak at ~289 eV (Figure S15) indicates the formation of a majority of -CO₃ and -CHF-O-CO₂- within the SEI, aligning with previous findings [24,47]. As per the F 1 s spectra (Fig. 2j-1), it is apparent that NaF was produced within the SEI during formation, with varying concentrations of FEC.

Following formation, the cells underwent two cycles at C/20 before being stored under open circuit voltage conditions for the subsequent 500 hours at 4.0 V and 40°C. Cells containing 5 wt% and 10 wt% FEC exhibit comparable voltage drops during storage (Fig. 3a). Nonetheless, these voltage drops are slightly smaller than that observed in the 2 wt% FEC containing cell. This suggests that the CEI in cells with 5 wt% and 10 wt% FEC performs better in preventing electrolyte oxidation at the cathode side. The volume of gas produced was recorded after 500 hours of storage at 40°C, as shown in Fig. 3b. Notably, regardless of the concentrations of FEC additive, all cells exhibited a significant amount of gas production (>3 mL). Fig. 3c shows the post-storage Nyquist plot measured at 3.1 V and 25°C. In comparison to the Rct observed after formation at 3.1 V (Supplementary Table 2), the Rct values for 2 wt%, 5 wt%, and 10 wt% increased by 38.48 $\Omega \times \text{cm}^2$, 67.51 $\Omega \times \text{cm}^2$, and 93.15 $\Omega \times \text{cm}^2$, respectively, during storage.

To evaluate the impact of the newly developed EA-based electrolyte systems on the cycling lifespan of SIBs, the pouch cells were subjected to testing with a rate of C/3 in CCCV mode with a C/20 cut-off current between 1.5 and 4.0 V at 40°C with periodic C/20 check-up cycles every 50 cycles. All the cells show 250 cycles with $\sim\!80$ % capacity retention (Fig. 3d). Cells with different concentrations of FEC additive display similar capacity fade trends (Fig. 3d), despite having distinct R_{ct} values prior to cycling (Fig. 3c). This consistency is further confirmed by the plot of normalized discharge capacity versus cycling number (Figure S16). Importantly, all cells exhibit similar capacity retention during each slow check-up cycle, minimizing the effect of impedance (Figure \$16). This suggests the presence of a universal failure mechanism driving the capacity degradation across all cells in this study. In order to comprehend the failure mechanism of these cells, EIS coupled with equivalent circuit fitting was utilized to examine the changes in Rct values during long-term cycling (Fig. 3e). A notable increase in Rct is observed for cells containing 2 wt% FEC (222 $\Omega \times \text{cm}^2$), 5 wt% FEC (226 $\Omega \times \text{cm}^2$), and 10 wt% FEC (350.7 $\Omega \times \text{cm}^2$) even at 25°C. To unravel the source of impedance growth, symmetric cells were constructed to analyze the changes in Rct at both the NCMFNZO cathode (Fig. 3f) and HC anode (Fig. 3g). With 10 wt% FEC, the highest R_{ct} values were recorded at both the cathode and anode compared to those of 2 wt% and 5 wt% FEC containing cells. As a side note, the significant impedance changes on the cathode side during cycling (Figs. 2e and 3f) resemble those observed in lithium-ion layered oxide cathodes. These changes could be attributed to surface reconstruction and chemical evolution [48]. Further studies on sodium-ion layered oxide cathodes are encouraged to deconvolute R_{ct} and better understand the impedance contributions. Interestingly, severe sodium plating was observed across all HC anodes (Figure S17), despite varying R_{ct} values (Fig. 3g), when the cells were opened to fabricate symmetric cells. The deposited sodium metal has the potential to react with electrolyte, leading to the consumption of active sodium and electrolyte. Consequently, this results in the capacity degradation across all the cells studied here. Given that undesirable sodium plating may arise from an elevated resistance of the

SEI and sluggish charge transfer kinetics [49,50], XPS analysis was conducted on the HC anode post-cycling (Fig. 3h-j, S18) to understand the interphasial chemistry changes. In comparison to the SEI chemistries observed after formation (Fig. 2j-I), the proportion of C-F is greater than that of NaF across all samples after cycling (Fig. 3h-j). This observation suggests that organic species begin to accumulate in the SEI during cycling, which could be a contributing factor to the increased R_{ct} values.

Gas evolution issues during cycling or storage at the pouch cell level are a common challenge faced by SIBs [26]. By utilizing the developed simple electrolyte system consisting of 1 m NaPF₆ in EA with 5 wt% FEC, the source of gas evolution at various temperatures, including -18°C, 25°C, and 40°C, was identified using pouch bag methodology [51] to isolate cathode and anode (Fig. 4a-b, S19). Gas evolution primarily occurs due to the interactions between the cathode and electrolytes (Fig. 4a). At a temperature of 40° C, ~ 6.5 mL of gas was produced after 100 hours of storage, maintaining this level consistently throughout the 500-hour testing period. As the temperature drops to 25°C, the rate of gas generation slows down, eventually resulting in the gradual production of ~ 6 mL of gas after 500 hours of storage. At a temperature of -18°C, there is virtually no gas generated. This demonstrates that temperature significantly influences the rate of gas evolution, with higher temperatures accelerating the process and lower temperatures impeding it. In contrast, no gas generation is observed from the reactions between the sodiated HC anode and electrolytes (Fig. 4b). When comparing to 25°C, the volume of the pouch bag exhibits a negative value at both -18° C and 40° C, indicating a decrease in pouch bag volume. This reduction in volume is easily understandable at −18°C, as objects typically shrink at lower temperatures. The decrease in volume at 40°C could be attributed to the consumption of sodium and electrolyte during the increase in side reactions at higher temperatures.

To further investigate gas evolution in relation to the upper-cutoff voltage, cells containing 1 m NaPF₆ in EA with 5 wt% FEC were held at various voltages for 5 hours each. The subsequent evolution of gas volume was then measured. Surprisingly, no significant amount of gas was generated until the voltage reached 4.0 V (Fig. 4c). CO2 and DMC are identified as the major gas components using GC-MS analysis (Figure S20). It is highly probable that DMC originates from the residue of the GC column due to previous battery electrolyte analysis (Figure S20), rather than being generated by the reactions between electrode and EA-based electrolyte, as there is a lack of methoxide to convert EA to DMC. DFT calculations were performed (Fig. 4d-g), focusing on a chosen set of reactions occurring at a comparatively low oxidation potential, aiming to achieve a mechanistic understanding of the pathways leading to CO2 generation. An interesting mechanism involving hydrogen transfer from FEC or EA to carbonates is postulated (Fig. 4d, e, g). The mechanisms in Fig. 4d and g show only the hydrogen transfer step, the radical may then undergo oligomerization or other downstream processes. Fig. 4e is noteworthy in that FEC is converted to VC. NaF and a bicarbonate radical (confirmed by spin densities) are generated in this process as well. The bicarbonate radical decomposes to CO₂ and the extremely reactive hydroxyl radical. It is also found that the FEC after hydrogen transfer may be susceptible to ring-opening and elimination of CO₂. Additional reactions are covered in Figure S21, which examine hydrogen transfer between homodimers (EA-EA, FEC-FEC) and heterodimers (EA-FEC, EA-PF₆, FEC-PF₆). Intrinsic oxidation potentials for EA (6.44 V vs Na⁺/Na) and FEC (7.45 V vs Na⁺/Na) are reported as well, further emphasizing the importance of the consideration of chemical processes occurring in concert with oxidation. It is noteworthy that the gas generated from pouch cells (Fig. 4c) is notably less than that from cathode-electrolyte reactions (Fig. 4a), indicating gas consumption by the HC anode, aligning with prior findings [26].

As an exploratory study, the impact of EA-based electrolyte systems under extreme conditions, including fast charging and low temperatures, was investigated. Using 1 m NaPF $_6$ in EA with 5 wt% FEC as a representative electrolyte, fast charging tests were conducted at 25°C with various charging rates including C/3, 1 C, 2 C, 3 C, and 4 C.

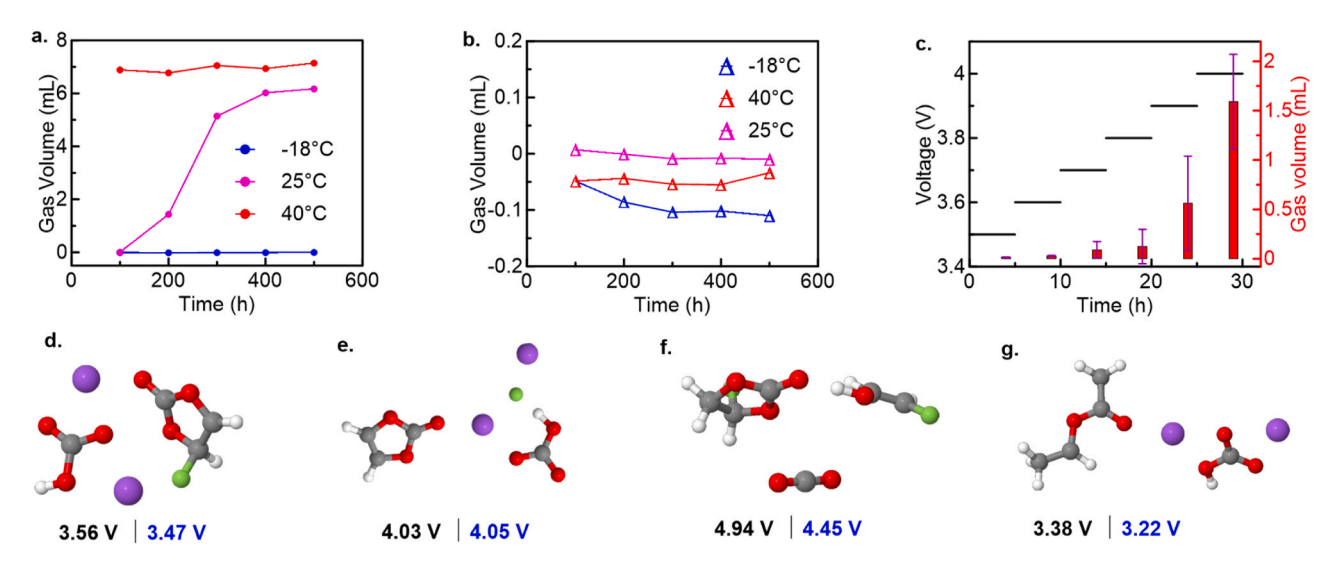


Fig. 4. Evaluation of the gas evolution of NCMFNZO/HC pouch cells with 1 m NaPF₆ in EA + 5 wt% FEC. Gas volume versus time at different temperatures for pouch bags containing (a) the desodiated NCMFNZO electrode with electrolyte or (b) sodiated HC electrode with electrolyte. All the electrodes were taken from NCMFNZO/HC pouch cells having an initial voltage of 4.0 V. (c) Gas volume generated with corresponding upper cut-off voltages for NCMFNZO/HC pouch cells. Each cell was held at specific voltages for 5 hours, with gas volume quantified immediately afterward. The error bars denote the variance between measurements from two individual cells. (d-g) DFT calculations on the potential pathways of generating CO_2 gas. Oxidation potentials (in the Na $^+$ /Na scale) for FEC (d-f) and EA (g), computed with the SMD(ether) B97XD/CBSB7 $^+$ + model chemistry (value in black) and SMD(ether) G4MP2 model chemistry (value in blue). The relationship between full cell voltage and potentials (in the Na $^+$ /Na scale) can be referred to the previous work [26].

Discharging was performed at C/3 for each cycle, with a C/20 check-up every 10 cycles to assess any sodium inventory loss potentially caused by sodium plating during fast charging. Upon reaching a charging rate of 2 C, a notable capacity loss, including during the check-up cycles, was observed (Fig. 5a). This suggests the occurrence of sodium plating on the HC anode, which was confirmed by opening cells after cycling at 2 C (Fig. 5b). ARC was subsequently conducted to examine the impact of sodium plating on the thermal stability performance of the cell (Fig. 5c). Two tests were carried out for each specimen to ensure repeatability. Cells exhibiting sodium plating were obtained by subjecting them to 10 cycles with a charging rate of 2 C after formation. In comparison to cells after formation without sodium plating, those with sodium plating displayed a significant exothermic peak at around 100°C (Fig. 5c). Subsequently, their self-heating rate (SHR) was found to be similar to that of cells without sodium plating. This indicates safety concerns associated with sodium plating in SIBs.

Subsequently, 1 m NaPF₆ in EA with 5 wt% FEC was employed as a representative electrolyte to investigate the low-temperature performance, including conditions at 10° C, 0° C, and -10° C, within the voltage range of 1.5-4.0 V at C/3 (Fig. 5d). A significant capacity loss, possibly induced by sodium plating, was observed starting at 0°C (Fig. 5d). Cycling at 10°C appeared to be manageable at C/3. It is noteworthy to further examine the occurrence of sodium plating at 10°C with varying charging rates. Cells with varying R_{ct} values including 170.9, 232.8, and 277.6 $\Omega \times \text{cm}^2$ were obtained by using different concentrations of FEC additive (Fig. 5e). Two different charging C-rates, C/5 and C/2.5, were chosen for cycling up to 3.8 V at 10°C (Fig. 5f), as electrolyte oxidation and transition metal dissolution at the cathode side are negligible under these conditions [52]. Thus, any rapid capacity loss during cycling at 10°C would likely be attributed to unwanted sodium plating. Discharging was conducted at C/3 for each cycle. During the initial 40 cycles at C/5, there was minimal capacity loss observed. However, significant capacity loss occurred when the charging rate was increased to C/2.5, irrespective of the initial R_{ct} values. No further capacity loss was observed once the charging rate was reduced back to C/5 to mitigate further sodium plating. It is probable that the initial R_{ct} values across all the cells had exceeded the threshold for sodium plating. To mitigate sodium plating, further exploration of additives in the future to further decrease R_{ct}, particularly on the HC anode side, may be warranted to extend cell lifetime during fast charging or at low temperatures.

4. Conclusions

In this work, the successful cycling of NCMFNZO/HC pouch cells filled with EA as the sole solvent with FEC as film-forming electrolyte additives, has been demonstrated. FTIR, MD simulations, and pfg-NMR analyses confirmed the weakly solvating structure of Na⁺ ions with EA, along with a competitive diffusion coefficient of $3.95 \times 10^{-10} \text{ m}^2 \text{ s}^{-1}$. By incorporating various concentrations of FEC additive, these EA-based electrolytes achieved a lifetime of 250 cycles with \sim 80 % capacity retention when cycled up to $4.0\,\mathrm{V}$ at $40^{\circ}\mathrm{C}$ with C/3. Utilizing this straightforward EA-based electrolyte system facilitated an in-depth examination of SIBs failure mechanisms, particularly focusing on impedance growth, sodium plating, and gas evolution. Significant growth in Rct was observed on both the NCMFNZO cathode and HC anode. Particularly, as more organic species formed in the SEI, the increase in R_{ct} at the HC anode side led to the occurrence of sodium plating. Such plating adversely affected cell lifespan, particularly during room temperature fast charging exceeding 2 C or cycling at low temperatures below 10°C. Severe exothermic reactions around ~100°C in SIBs with sodium plating were identified by ARC. Regarding gas evolution, almost all the gas primarily comprised CO2 resulting from reactions between the NCMFNZO cathode and electrolytes. The quantity of gas demonstrated a correlation with the upper cutoff voltage and temperature. Higher voltages or temperatures resulted in increased gas generation.

This work unveils a novel class of low-cost ester-based solvents that facilitate the operation of SIBs. Further advancements in engineering to fine-tune the interphasial chemistry are necessary to mitigate impedance growth and gas evolution. This holds significant promise for future SIBs with exceptionally long lifetimes, catering to grid energy storage applications.

CRediT authorship contribution statement

Fuead Hasan: Data curation. Michel Johnson: Data curation. Chanmonirath (Michael) Chak: Data curation. Lin Ma: Writing – review & editing, Writing – original draft, Supervision, Funding acquisition, Conceptualization. Vadim Shipitsyn: Data curation. Wenhua

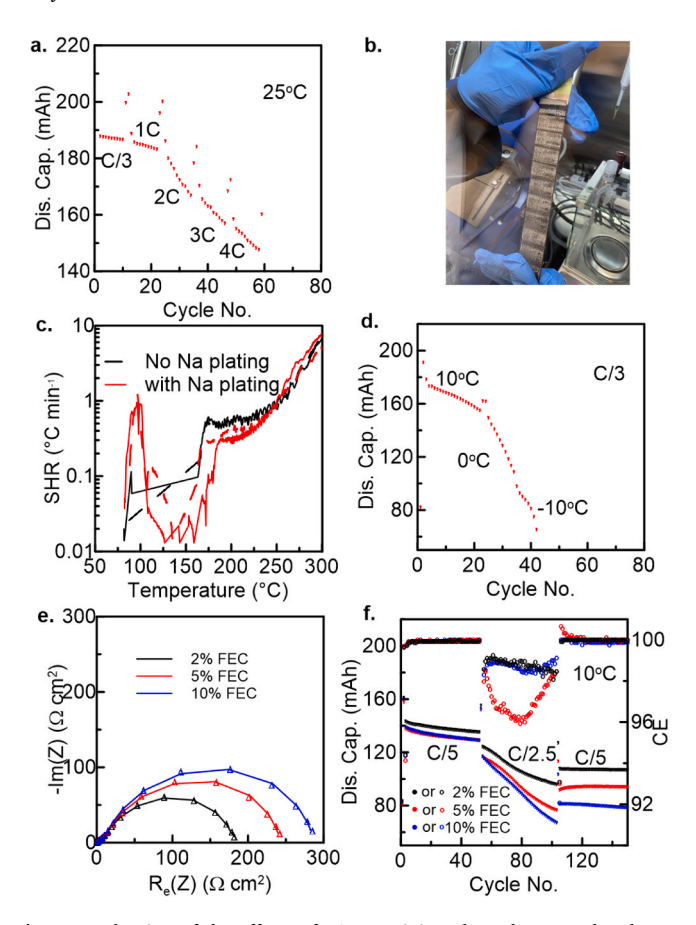


Fig. 5. Evaluation of the effects of EA containing electrolytes on the electrochemical performance of NCMFNZO/HC pouch cells under extreme conditions. (a) Discharge capacity vs. cycling No. during long-term cycling between 1.5 and 4.0 V at 25°C with different charging rates as labeled. Each cell was cycled at its respective rate for 10 cycles, with a discharging rate of C/3 utilized for each cycle. C/20 was performed every 10 cycles. (b) A picture of HC anode showing Na plating after 2 C cycling in (a). (c) SHR vs. temperature for NCMFNZO/HC pouch cells with 1 m NaPF $_6$ in EA + 5 wt% FEC at 4.0 V after formation or fast charging cycling with Na plating. Each ARC testing includes two pouch cells. (d) Discharge capacity vs. cycling No. during long-term cycling between 1.5 and 4.0 V at C/3 with different temperatures as labeled. The electrolyte of 1 m $NaPF_6$ in EA + 5 wt% FEC was used in (a-d). (e) The Nyquist plot after formation measured at 3.1 V and 10°C with equivalent circuit fitting. Experimental data are shown as solid line and fitted data are shown as triangle symbol. (f) Discharge capacity vs. cycling No. during long-term cycling between 1.5 and 3.8 V at 10°C with different cycling rates as labeled. C/20 was performed every 40 cycles.

Zuo: Writing – review & editing, Data curation. Glenn Pastel: Writing – review & editing, Supervision, Data curation. Travis P. Pollard: Writing – review & editing, Supervision, Data curation. Marshall A. Schroeder: Data curation. Christopher M. Beiger: Supervision. Rishivandhiga Jayakumar: Writing – original draft, Data curation, Conceptualization. Steve G. Greenbaum: Supervision, Data curation. Oleg Borodin: Writing – review & editing, Data curation. Allen Zheng: Data curation.

Declaration of Competing Interest

The authors declare the following financial interests/personal relationships which may be considered as potential competing interests: Lin Ma reports financial support, administrative support, and equipment, drugs, or supplies were provided by UNC Charlotte. Lin Ma reports financial support was provided by National Science Foundation. N/A If there are other authors, they declare that they have no known competing financial interests or personal relationships that could have

appeared to influence the work reported in this paper.

Data Availability

Data will be made available on request.

Acknowledgements

Dr. L.M. at UNC Charlotte acknowledges the support by the US National Science Foundation Award No. 2301719 and ORAU Ralph E. Powe Junior Faculty Enhancement Award. Dr. W. Z. at the Argonne National Laboratory acknowledges the support from the US Department of Energy, Vehicle Technologies Office. Modeling work was supported by DEVCOM ARL.

Conflicts of interest

There are no conflicts to declare.

Appendix A. Supporting information

Supplementary data associated with this article can be found in the online version at doi:10.1016/j.nanoen.2024.109969.

References

- [1] H.C. Hesse, M. Schimpe, D. Kucevic, A. Jossen, Lithium-Ion Battery Storage for the Grid—A Review of Stationary Battery Storage System Design Tailored for Applications in Modern Power Grids, Energies 10 (12) (2017) 2107.
- [2] D. Lu, R. Li, M.M. Rahman, P. Yu, L. Lv, S. Yang, Y. Huang, C. Sun, S. Zhang, H. Zhang, J. Zhang, X. Xiao, T. Deng, L. Fan, L. Chen, J. Wang, E. Hu, C. Wang, X. Fan, Ligand-channel-enabled ultrafast Li-ion conduction, Nature 627 (8002) (2024) 101–107.
- [3] G.A. Campbell, The cobalt market revisited, Miner. Econ. 33 (1) (2020) 21-28.
- [4] G. Mishra, R. Jha, A. Meshram, K.K. Singh, A review on recycling of lithium-ion batteries to recover critical metals, J. Environ. Chem. Eng. 10 (6) (2022) 108534.
- [5] P.K. Nayak, L. Yang, W. Brehm, P. Adelhelm, From Lithium-Ion to Sodium-Ion Batteries: Advantages, Challenges, and Surprises, Angew. Chem. Int. Ed. 57 (1) (2018) 102–120.
- [6] T. Chen, B. Ouyang, X. Fan, W. Zhou, W. Liu, K. Liu, Oxide cathodes for sodium-ion batteries: Designs, challenges, and perspectives, Carbon Energy 4 (2) (2022) 170–199.
- [7] J. Peng, W. Zhang, Q. Liu, J. Wang, S. Chou, H. Liu, S. Dou, Prussian blue analogues for sodium-ion batteries: past, present, and future, Adv. Mater. 34 (15) (2022) 2108384.
- [8] Y. Jin, P.M.L. Le, P. Gao, Y. Xu, B. Xiao, M.H. Engelhard, X. Cao, T.D. Vo, J. Hu, L. Zhong, B.E. Matthews, R. Yi, C. Wang, X. Li, J. Liu, J.-G. Zhang, Low-solvation electrolytes for high-voltage sodium-ion batteries, Nat. Energy 7 (8) (2022) 718–725.
- [9] C. Li, H. Xu, L. Ni, B. Qin, Y. Ma, H. Jiang, G. Xu, J. Zhao, G. Cui, Nonaqueous liquid electrolytes for sodium-ion batteries: fundamentals, progress and perspectives, Adv. Energy Mater. 13 (40) (2023) 2301758.
- [10] H.-J. Liang, H.-H. Liu, X.-X. Zhao, Z.-Y. Gu, J.-L. Yang, X.-Y. Zhang, Z.-M. Liu, Y.-Z. Tang, J.-P. Zhang, X.-L. Wu, Electrolyte chemistry toward ultrawide-temperature (-25 to 75 °C) sodium-ion batteries achieved by phosphorus/silicon-synergistic interphase manipulation, J. Am. Chem. Soc. 146 (11) (2024) 7295–7304.
- [11] X. Zhou, X. Chen, Z. Yang, X. Liu, Z. Hao, S. Jin, L. Zhang, R. Wang, C. Zhang, L. Li, X. Tan, S.-L. Chou, Anion receptor weakens ClO4— solvation for high-temperature sodium-ion batteries, Adv. Funct. Mater. 34 (5) (2024) 2302281.
- [12] G.G. Eshetu, T. Diemant, M. Hekmatfar, S. Grugeon, R.J. Behm, S. Laruelle, M. Armand, S. Passerini, Impact of the electrolyte salt anion on the solid electrolyte interphase formation in sodium ion batteries, Nano Energy 55 (2019) 327–340.
- [13] D. Ba, Q. Gui, W. Liu, Z. Wang, Y. Li, J. Liu, Robust cathode-ether electrolyte interphase on interfacial redox assembled fluorophosphate enabling high-rate and ultrastable sodium ion full cells, Nano Energy 94 (2022) 106918.
- [14] S.L. Dreyer, F.M. Maddar, A. Kondrakov, J. Janek, I. Hasa, T. Brezesinski, Elucidating gas evolution of prussian white cathodes for sodium-ion battery application: the effect of electrolyte and moisture, Batter. Supercaps 7 (2024) e202300595.
- [15] L. Zhang, C. Tsolakidou, S. Mariyappan, J.-M. Tarascon, S. Trabesinger, Unraveling gas evolution in sodium batteries by online electrochemical mass spectrometry, Energy Storage Mater. 42 (2021) 12–21.
- [16] Z. Tian, Y. Zhang, J. Zhu, Q. Li, T. Liu, M. Antonietti, A Reanalysis of the Diverse Sodium Species in Carbon Anodes for Sodium Ion Batteries: A Thermodynamic View, Adv. Energy Mater. 11 (47) (2021) 2102489.
- [17] J. Hedman, R. Mogensen, R. Younesi, F. Björefors, Fiber optic sensors for detection of sodium plating in sodium-ion batteries, ACS Appl. Energy Mater. 5 (5) (2022) 6219–6227.

- [18] R. Petibon, J. Harlow, D.B. Le, J.R. Dahn, The use of ethyl acetate and methyl propanoate in combination with vinylene carbonate as ethylene carbonate-free solvent blends for electrolytes in Li-ion batteries, Electrochim. Acta 154 (2015) 227-234
- [19] R. Petibon, C.P. Aiken, L. Ma, D. Xiong, J.R. Dahn, The use of ethyl acetate as a sole solvent in highly concentrated electrolyte for Li-ion batteries, Electrochim. Acta 154 (2015) 287–293.
- [20] M.C. Smart, B.V. Ratnakumar, S. Surampudi, Use of organic esters as cosolvents in electrolytes for lithium-ion batteries with improved low temperature performance, J. Electrochem. Soc. 149 (4) (2002) A361.
- [21] M.C. Smart, B.V. Ratnakumar, K.B. Chin, L.D. Whitcanack, Lithium-ion electrolytes containing ester cosolvents for improved low temperature performance, J. Electrochem. Soc. 157 (12) (2010) A1361.
- [22] X. Ma, R.S. Arumugam, L. Ma, E. Logan, E. Tonita, J. Xia, R. Petibon, S. Kohn, J. R. Dahn, A study of three ester Co-solvents in lithium-ion cells, J. Electrochem. Soc. 164 (14) (2017) A3556.
- [23] R. Mogensen, S. Colbin, R. Younesi, An attempt to formulate non-carbonate electrolytes for sodium-ion, Batter. Batter. Supercaps 4 (5) (2021) 791–814.
- [24] M. Carboni, J. Manzi, A.R. Armstrong, J. Billaud, S. Brutti, R. Younesi, Analysis of the Solid Electrolyte Interphase on Hard Carbon Electrodes in Sodium-Ion Batteries, ChemElectroChem 6 (6) (2019) 1745–1753.
- [25] V. Shipitsyn, R. Jayakumar, W. Zuo, W. Yin, E. Huber, L. Ma, The impact of fluoroethylene carbonate additive on charged sodium ion electrodes/electrolyte reactivity studied using accelerating rate calorimetry, J. Electrochem. Soc. 170 (11) (2023) 110501.
- [26] H. Hijazi, Z. Ye, L. Zhang, J. Deshmukh, M.B. Johnson, J.R. Dahn, M. Metzger, Impact of sodium metal plating on cycling performance of layered oxide/hard carbon sodium-ion pouch cells with different voltage cut-offs, J. Electrochem. Soc. 170 (7) (2023) 070512.
- [27] C.P. Aiken, J. Xia, D.Y. Wang, D.A. Stevens, S. Trussler, J.R. Dahn, An apparatus for the study of in situ gas evolution in Li-ion pouch cells, J. Electrochem. Soc. 161 (10) (2014) A1548.
- [28] R. Petibon, L.M. Rotermund, J.R. Dahn, Evaluation of phenyl carbonates as electrolyte additives in lithium-ion batteries, J. Power Sources 287 (2015) 184-195
- [29] Frisch, M.J.; Trucks, G.W.; Schlegel, H.B.; Scuseria, G.E.; Robb, M.A.; Cheeseman, J.R.; Scalmani, G.; Barone, V.; Petersson, G.A.; Nakatsuji, H.; Li, X.; Caricato, M.; Marenich, A.V; Bloino, J.; Janesko, B.G.; Gomperts, R.; Mennucci, B.; Hratchian, H. P.; Ortiz, J.V.; Izmaylov, A.F.; Sonnenberg, J.L.; Williams; Ding, F.; Lipparini, F.; Egidi, F.; Goings, J.; Peng, B.; Petrone, A.; Henderson, T.; Ranasinghe, D.; Zakrzewski, V.G.; Gao, J.; Rega, N.; Zheng, G.; Liang, W.; Hada, M.; Ehara, M.; Toyota, K.; Fukuda, R.; Hasegawa, J.; Ishida, M.; Nakajima, T.; Honda, Y.; Kitao, O.; Nakai, H.; Vreven, T.; Throssell, K.; Montgomery Jr., J.A.; Peralta, J.E.; Ogliaro, F.; Bearpark, M.J.; Heyd, J.J.; Brothers, E.N.; Kudin, K.N.; Staroverov, V.N.; Keith, T.A.; Kobayashi, R.; Normand, J.; Raghavachari, K.; Rendell, A.P.; Burant, J.C.; Iyengar, S.S.; Tomasi, J.; Cossi, M.; Millam, J.M.; Klene, M.; Adamo, C.; Cammi, R.; Ochterski, J.W.; Martin, R.L.; Morokuma, K.; Farkas, O.; Foresman, J.B.; Fox, D.J. Gaussian 16 Rev. C.01 , Wallingford, CT, 2016.
- [30] P. Pracht, F. Bohle, S. Grimme, Automated exploration of the low-energy chemical space with fast quantum chemical methods, Phys. Chem. Chem. Phys. 22 (14) (2020) 7169–7192.
- [31] W.M. Haynes. CRC Handbook of Chemistry and Physics, 94th Ed., CRC Press, 2016.
- [32] P.K. Muhuri, D.K. Hazra, Density and Viscosity for Propylene Carbonate + 1,2-Dimethoxyethane at 298.15, 308.15, and 318.15 K, J. Chem. Eng. Data 39 (2) (1994) 375–377
- [33] S.P. Verevkin, A.V. Toktonov, Y. Chernyak, B. Schäffner, A. Börner, Vapour pressure and enthalpy of vaporization of cyclic alkylene carbonates, Fluid Phase Equilib. 268 (1) (2008) 1–6.

[34] K. Hayamizu, Y. Aihara, S. Arai, C.G. Martinez, Pulse-gradient spin-echo H-1, Li-7, and F-19 NMR diffusion and ionic conductivity measurements of 14 organic electrolytes containing LiN(SO2CF3)(2), J. Phys. Chem. B 103 (3) (1999) 519–524.

Nano Energy 128 (2024) 109969

- [35] O. Borodin, Polarizable Force Field Development and Molecular Dynamics Simulations of Ionic Liquids, J. Phys. Chem. B 113 (33) (2009) 11463–11478.
- [36] S.-D. Han, O. Borodin, D.M. Seo, Z.-B. Zhou, W.A. Henderson, Electrolyte Solvation and Ionic Association: V. Acetonitrile-Lithium Bis(fluorosulfonyl)imide (LiFSI) Mixtures, J. Electrochem. Soc. 161 (14) (2014) A2042–A2053.
- [37] O. Borodin, G.D. Smith, Quantum chemistry and molecular dynamics simulation study of dimethyl carbonate: ethylene carbonate electrolytes doped with LiPF6, J. Phys. Chem. B 113 (6) (2009) 1763–1776.
- [38] R. Andersson, O. Borodin, P. Johansson, Dynamic structure discovery applied to the ion transport in the ubiquitous lithium-ion battery electrolyte LP30, J. Electrochem. Soc. 169 (10) (2022) 100540.
- [39] G.D. Smith, O. Borodin, S.P. Russo, R.J. Rees, A.F. Hollenkamp, A molecular dynamics simulation study of LiFePO₄/electrolyte interfaces: structure and Li⁺ transport in carbonate and ionic liquid electrolytes, Phys. Chem. Chem. Phys. 11 (42) (2009) 9884–9897.
- [40] A.V. Cresce, S.M. Russell, O. Borodin, J.A. Allen, M.A. Schroeder, M. Dai, J. Peng, M.P. Gobet, S.G. Greenbaum, R.E. Rogers, K. Xu, Solvation behavior of carbonate-based electrolytes in sodium ion batteries, Phys. Chem. Chem. Phys. 19 (1) (2017) 574–586.
- [41] P. Wróbel, A. Eilmes, Effects of Me–solvent interactions on the structure and infrared spectra of MeTFSI (Me = Li, Na) solutions in carbonate solvents—a test of the GFN2-xTB approach in molecular dynamics simulations, Molecules 28 (18) (2023) 6736.
- [42] L. Suo, O. Borodin, T. Gao, M. Olguin, J. Ho, X. Fan, C. Luo, C. Wang, K. Xu, "Water-in-salt" electrolyte enables high-voltage aqueous lithium-ion chemistries, Science 350 (6263) (2015) 938–943.
- [43] A.S. Keefe, S. Buteau, I.G. Hill, J.R. Dahn, Temperature dependent EIS studies separating charge transfer impedance from contact impedance in lithium-ion symmetric cells, J. Electrochem. Soc. 166 (14) (2019) A3272.
- [44] J. Landesfeind, J. Hattendorff, A. Ehrl, W.A. Wall, H.A. Gasteiger, Tortuosity DEtermination of Battery Electrodes and Separators by Impedance Spectroscopy, J. Electrochem. Soc. 163 (7) (2016) A1373.
- [45] L. Madec, J. Xia, R. Petibon, K.J. Nelson, J.-P. Sun, I.G. Hill, J.R. Dahn, Effect of sulfate electrolyte additives on LiNi_{1/3}Mn_{1/3}Co_{1/3}O₂/graphite pouch cell lifetime: correlation between XPS surface studies and electrochemical test results, J. Phys. Chem. C. 118 (51) (2014) 29608–29622.
- [46] P. Bai, X. Han, Y. He, P. Xiong, Y. Zhao, J. Sun, Y. Xu, Solid electrolyte interphase manipulation towards highly stable hard carbon anodes for sodium ion batteries, Energy Storage Mater. 25 (2020) 324–333.
- [47] M. Dahbi, T. Nakano, N. Yabuuchi, S. Fujimura, K. Chihara, K. Kubota, J.-Y. Son, Y.-T. Cui, H. Oji, S. Komaba, Effect of hexafluorophosphate and fluoroethylene carbonate on electrochemical performance and the surface layer of hard carbon for sadium-ion batteries. Chem ElectroChem. 3 (11) (2016) 1856–1867.
- [48] F. Lin, I.M. Markus, D. Nordlund, T.-C. Weng, M.D. Asta, H.L. Xin, M.M. Doeff, Surface reconstruction and chemical evolution of stoichiometric layered cathode materials for lithium-ion batteries, Nat. Commun. 5 (1) (2014) 3529.
- [49] B.V. Ratnakumar, M.C. Smart, S. Surampudi, Effects of SEI on the kinetics of lithium intercalation, J. Power Sources *97-98* (2001) 137–139.
- [50] N. Legrand, B. Knosp, P. Desprez, F. Lapicque, S. Raël, Physical characterization of the charging process of a Li-ion battery and prediction of Li plating by electrochemical modelling, J. Power Sources 245 (2014) 208–216.
- [51] D.J. Xiong, R. Petibon, M. Nie, L. Ma, J. Xia, J.R. Dahn, Interactions between Positive and Negative Electrodes in Li-Ion Cells Operated at High Temperature and High Voltage, J. Electrochem. Soc. 163 (3) (2016) A546.
- [52] Q.Q. Liu, R. Petibon, C.Y. Du, J.R. Dahn, Effects of electrolyte additives and solvents on unwanted lithium plating in lithium-ion cells, J. Electrochem. Soc. 164 (6) (2017) A1173.